Chinese Chemical Letters 36 (2025) 110185

Contents lists available at ScienceDirect

Chinese Chemical Letters

journal homepage: www.elsevier.com/locate/cclet

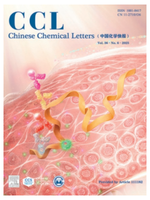

PVP decorated $H_{3.78}V_6O_{13}$ microspheres assembled by nanosheets for aqueous zinc ion batteries at variable work temperature

Chunru Zhao[a], Yi Liu[a], Shilong Li[a], Xiang Wu[a,*], Jinghai Liu[b,*]

[a] School of Materials Science and Engineering, Shenyang University of Technology, Shenyang 110870, China
[b] Inner Mongolia Engineering Research Center of Lithium-Sulfur Battery Energy Storage, College of Chemistry and Materials Science, Inner Mongolia Minzu University, Tongliao 028000, China

ARTICLE INFO

Article history:
Received 3 June 2024
Revised 14 June 2024
Accepted 27 June 2024
Available online 27 June 2024

Keywords:
Aqueous zinc ion batteries
Cathode materials
$H_{3.78}V_6O_{13}$ microspheres
Low temperature
High capacity

ABSTRACT

As a kind of emerging energy storage devices, Aqueous zinc ion batteries possess the characteristics of safety, low cost and environmental friendliness. However, their further application is restricted by the sluggish electrochemical reaction kinetics and low conductivity. In this work, we prepare two $H_{3.78}V_6O_{13}$ electrode materials with many active sites, which promotes the kinetics of ion diffusion and then improves the capacity of the cell. The as-obtained HVO-PVP electrode possess a capacity of 393.2 and 285.9 mAh/g at 0.2 and 5.0 A/g, respectively. Moreover, the assembled Zn//HVO-PVP cells also indicate excellent specific capacity and cycle stability at different operating temperatures (0–60 °C).

In recent years, the energy crisis and environmental pollution are two main challenges with the quick development of society [1]. Therefore, it is crucial to explore some renewable energy storage devices. Lithium-ion batteries (LIBs) have been widely applied and dominate the secondary energy market [2,3]. However, many issues still limit their further applications on large-scale, such as the scarce lithium resources and the safety of electrolytes [4]. Aqueous zinc-ion batteries (AZIBs) are expected to be alternatives to LIBs due to their nontoxicity, low potential and high theoretical capacity [5,6]. Currently, the investigation on cathode materials primarily focuses on manganese-based [7,8] and vanadium-based compounds [9,10], Prussian blue analogues [11,12] and metal-organic frameworks (MOFs) [13]. Nevertheless, the structural instability of manganese-based materials leads the capacity degradation during charging and discharging [14]. Prussian blue compounds present low theory capacity and poor conductivity [15]. It is difficult to precisely control the morphology of samples for MOF based electrodes [16]. Thus, it is imperious to develop many appropriate cathode materials with outstanding total performance.

Vanadium oxides have attracted considerable attention owning to their various valence states and large theoretical capacity [17,18]. Surfactant plays an important role in controlling the morphology of material. Among them, polyvinylpyrrolidone (PVP) can be employed as shape-controlling agent and surface stabilizer to increase the specific surface area [19,20]. For example, Cao and co-workers synthesized $H_{3.78}V_6O_{13}$ cathode for AZIBs with a capacity of 383.0 mAh/g at 0.2 A/g [21]. They maintain 111.0 mAh/g at the current density of 10.0 A/g. The fabricated PVP-VO_2 cells delivered a capacity of 470.2 mAh/g at 0.5 A/g [22]. Although some progresses have been made in capacity improvement, the cycle stability still needs to be maintained. Herein, we synthesize HVO-PVP sphere-like structures by one-step hydrothermal avenue. The Zn//HVO-PVP cells deliver the capacities of 393.2 and 285.9 mAh/g at 0.2 and 5.0 A/g, respectively. In addition, the capacity maintains 343.5 mAh/g at 1.0 A/g after 1000 times cycling at 0 °C. It demonstrates their potential application prospects in next generation portable energy storage systems.

In a typical procedure, 6 mmol of NH_4VO_3 powder and 0.3 g of PVP powder were subsequently put into 45 mL of deionized (DI) water and stirred at 80 °C. Then 8 mmol of $H_2C_2O_4 \cdot 2H_2O$ was dissolved into 15 mL of DI water and sonicated for 30 min. Then we poured the mixture into above mentioned solution and stirred for 30 min. Finally, the mixed solution was transferred into a 100 mL Teflon-lined autoclave and heated at 180 °C for 24 h. After cooling to room temperature, the solution was washed with alcohol and DI water several times and dried overnight at 60 °C. The collected powder was named as HVO-PVP. For comparison, the $H_{3.78}V_6O_{13}$ sample was prepared without the introduction of PVP and labeled as HVO.

---

* Corresponding authors.
E-mail addresses: wuxiang05@sut.edu.cn (X. Wu), jhliu2008@sinano.ac.cn (J. Liu).

https://doi.org/10.1016/j.cclet.2024.110185
1001-8417/

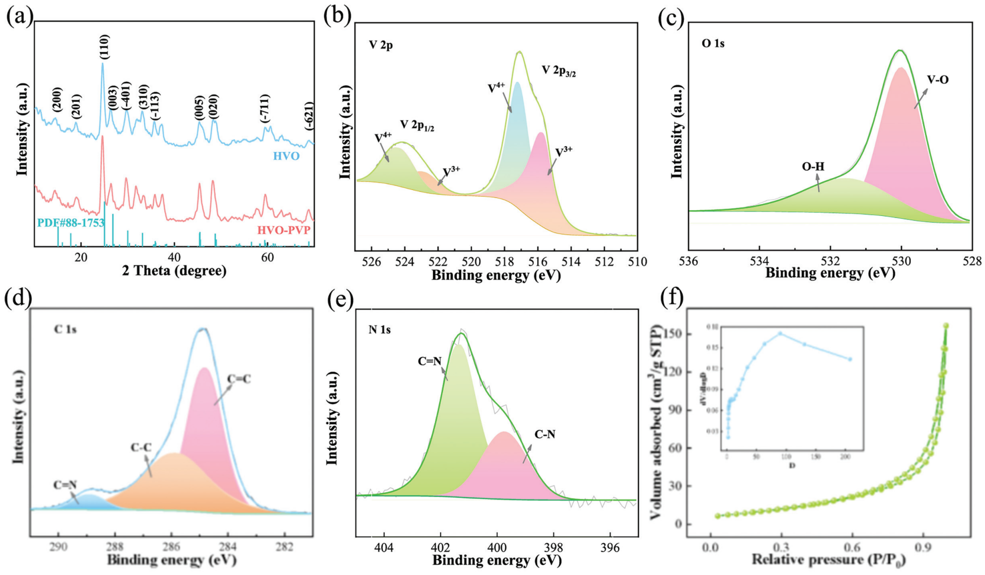

Fig. 1. Structural and compositional characterizations of as-prepared samples. (a) XRD patterns. (b) V 2p. (c) O 1s. (d) C 1s. (e) N 1s. (f) The N_2 adsorption-desorption isotherms.

X-ray diffraction analyzer (XRD, Shimadzu-7000) was utilized to investigate the phase and crystal structures of the samples. Then we evaluated elemental content and valence by X-ray photoelectron spectroscope (XPS, ESCALAB250Xi, Thermo Scientific). Their morphologies and microstructures were studied by scanning electron microscope (SEM, Hitachi, S-3400 N) and transmission electron microscope (TEM, FEI Tecnai F20). The specific surface area and pore size of the samples were calculated using Micromeritics ASAP *via* a Bruauer-Emmett-Teller (BET) approach.

Cathode materials were prepared by mixing the prepared samples with carbon black (Super P) and polyvinylidene fluoride (PVDF) in a mass ratio of 7:2:1. Subsequently, an appropriate amount of *N*-methyl-L-2-pyrrolidone (NMP) was then added in the above powder to form a slurry. After that, it was coated on a graphite paper and then dried overnight in a vacuum oven at 60 °C. Several CR2032 button cells in air were assembled by using zinc anode, glass fiber separator, as-prepared cathode and electrolyte (3 mol/L $Zn(CF_3SO_3)_2$), respectively. The positive materials possess an average loading mass of 1.5 mg. A Neware battery system (CT-4008T) was used to investigate the galvanostatic charge-discharge (GCD) curves, galvanostatic intermittent titration technique (GITT) and cyclic stability. Finally, we study the cyclic voltammetry (CV) and electrochemical impedance spectroscopy (EIS) through an electrochemical workstation (CHI660E).

Firstly, we evaluate the crystal structure and crystallinity of the samples. From XRD patterns in Fig. 1a, the diffraction peaks match well with $H_{3.78}V_6O_{13}$ phase (JCPDs No. 88–1753). Their lattice parameters are $a = 11.973$ Å, $b = 3.731$ Å and $c = 10.141$ Å. The typical peaks at 15.05°, 18.89°, 25.01°, 26.82°, 30.00°, 33.17°, 45.49°, 48.77° and 58.40° correspond to (200), (201), (110), (003), ($\bar{4}01$), (310), (005), (020) and ($\bar{7}11$). There are not additional phases appearing after the introduction of PVP. XPS is then utilized to study the composition and valence of the elements. The V 2p spectra (Fig. 1b) are de-convoluted into V^{3+} and V^{4+}, which correspond to 522.86 and 524.35 eV, respectively [23,24]. For O 1s spectra (Fig. 1c), two peaks at 531.50 and 530.00 eV can be assigned to O–H and V-O, respectively [25]. The C 1s spectra indicates the peaks at 284.78, 285.88 and 288.88 eV, belong to C=C, C–C and C=N, respectively (Fig. 1d) [26]. As for N 1s spectra (Fig. 1e), it can be fitted to two signal peaks, including C–N bonds at 399.75 eV, C=N bonds at 401.32 eV [27]. The presence of C–N bond shows that PVP is successfully introduced into HVO host materials [28]. From Fig. 1f, the HVO-PVP samples present the specific surface areas of 41.46 m^2/g and average pore diameters of 19.28 nm. The results demonstrate that PVP can improve the specific surface area of the HVO samples, which facilitates the transfer of zinc ions between electrode and electrolyte [29].

After that, we observe the morphology of the samples by SEM. From Figs. 2a and b, the HVO spheres consist of many stacked nanosheets with irregular shapes. However, regular nanosheets are assembled into micro-flowers after the addition of PVP (Figs. 2c and d). The exposed surfaces are expected to provide abundant active sites for superior rate performance [30]. Fig. 2e further demonstrates the micro-sphere shape of the HVO-PVP materials. The HRTEM image (Fig. 2f) indicates a lattice spacing of 0.354 nm, which corresponds to (110) crystal plane of the $H_{3.78}V_6O_{13}$ phase. The elemental mappings indicate a uniform distribution of V, O and C through the sphere (Figs. 2g-j).

Subsequently, a series of characterizations are performed to explore the electrochemical performance of the cells. The CV curves show two pairs of redox peaks in the voltage range from 0.2 V to 1.4 V (Fig. 3a). In the initial three cycles, the similar curve shape indicates their high reversibility during electrochemical reaction when the scanning rate is 0.1 mV/s. Fig. 3b presents the specific capacity of the two batteries at 0.2 A/g. During the first cycle, the HVO-PVP battery delivers a discharge capacity of 393.2 mAh/g. The discharge capacity remains at 362.9 mAh/g with a capacity retention of 92.3% after 90 times cycling. In comparison, the HVO electrode provides a specific capacity of 305.3 mAh/g. It suggests that PVP can improve the electrochemical performance of the electrode materials. The GCD curves of HVO-PVP samples demonstrate two charge-discharge platforms (Fig. 3c), which are consistent with the redox peaks (0.60/1.03 V and 0.50/1.01 V) of CV curves shown in Fig. 3a. The discharge platform at 0.4 V indicate their fast ion diffusion and small voltage polarization [31]. The rate capability of the battery is also a crucial parameter for assessing their practical applications. Fig. 3d shows the current density dependent specific capacity varying from 0.1 A/g to 5.0 A/g. The assembled Zn//HVO-PVP cells possess the specific capacities of 414.6, 395.9, 374.8, 353.4, 327.5 and 276.3 mAh/g at 0.1, 0.2, 0.5, 1.0, 2.0 and 5.0 A/g, respectively. They still keep the capacity of 402.8 mAh/g when the current density recovers to 0.1 A/g. This result confirms that the

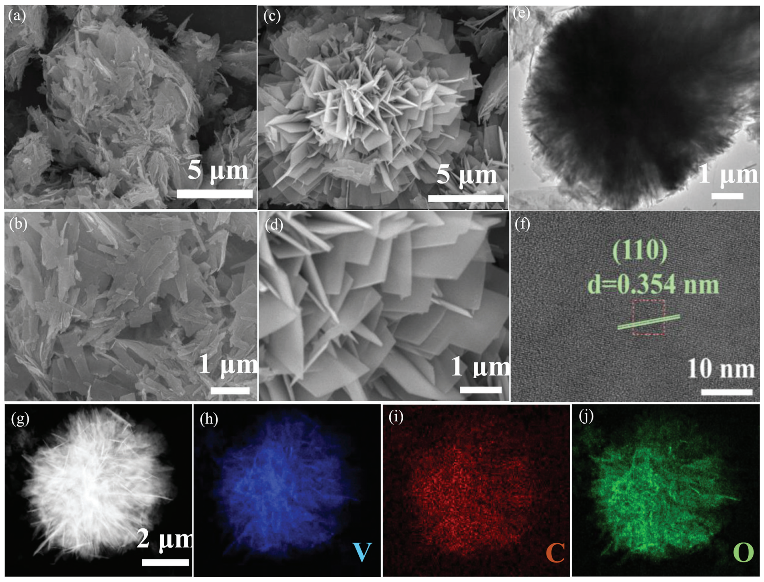

Fig. 2. Morphology characterization of all samples. SEM images of (a, b) HVO samples and (c, d) HVO-PVP samples. (e, f) TEM and HRTEM images of HVO-PVP products. (g-j) corresponding elements mappings of HVO-PVP sample.

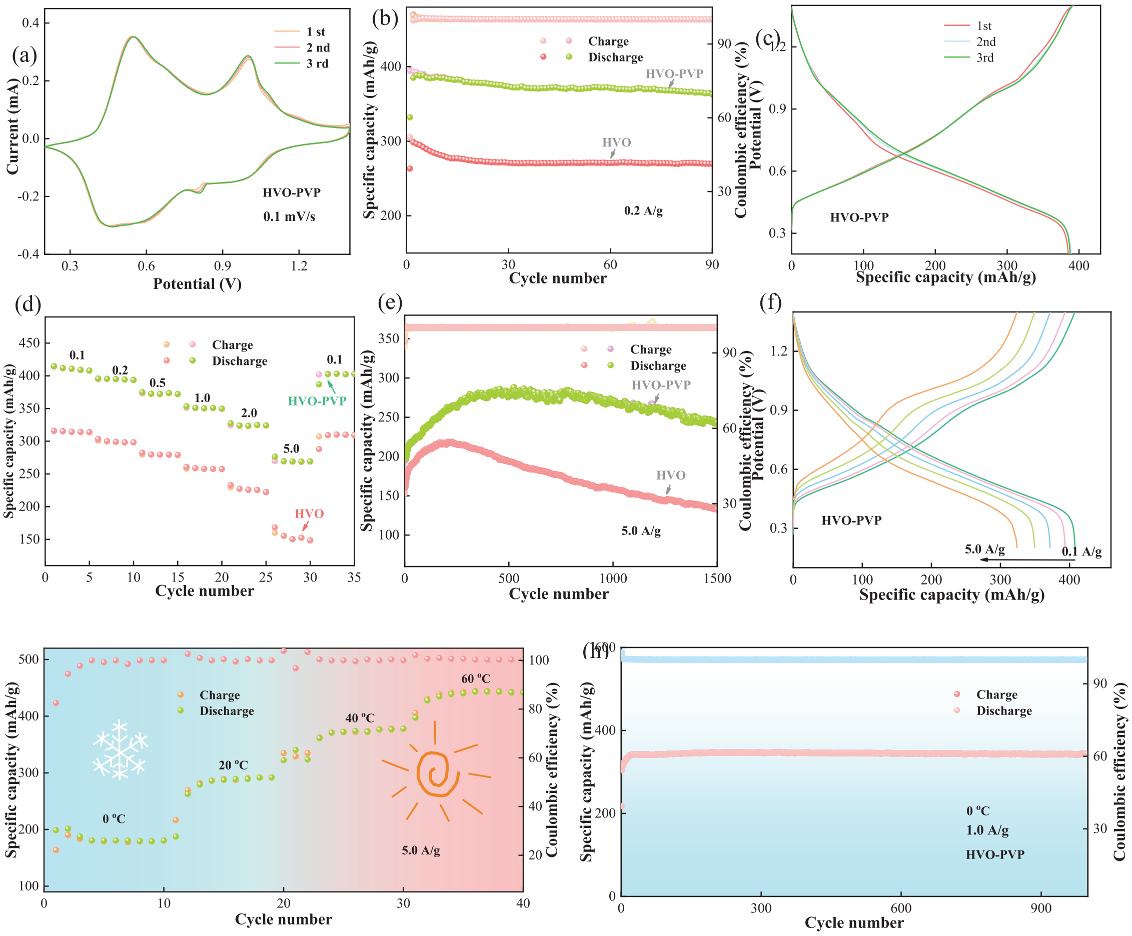

Fig. 3. Electrochemical performance. (a) CV curves of HVO-PVP electrode at 0.1 mV/s. (b) Cycling performance and (c) GCD curves of HVO-PVP electrodes at 0.1 A/g. (d) Rate capabilities of HVO and HVO-PVP electrodes at different current densities. (e) Long-term cycles at 5 A/g. (f) GCD curves at various current densities. (g) Cycling performance at different temperatures. (h) Cycling performance at 0 °C.

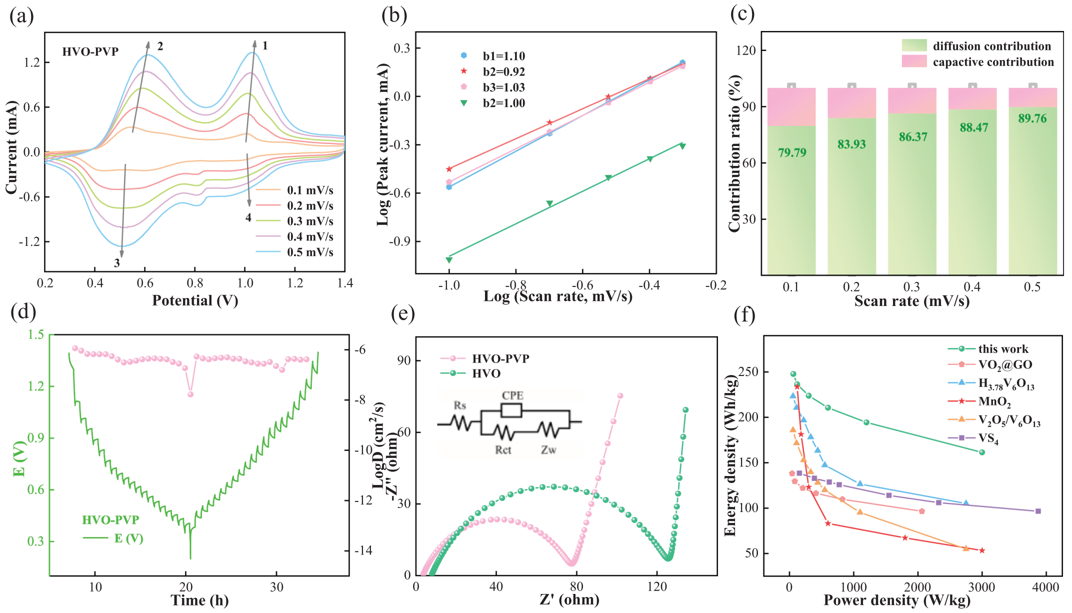

Fig. 4. Electrochemical reaction dynamics. (a) CV curves. (b) log(i) *versus* log(v). (c) Capacitive contribution ratios at various scan rates. (d) GITT curves. (e) Nyquist plots of HVO and HVO-PVP electrodes. (f) Ragone plot of HVO-PVP.

sheet-like structures provide many contacts area between active material and electrolyte [32].

From Fig. 3e, the HVO-PVP electrode presents a specific capacity of 285.9 mAh/g at 5.0 A/g with a corresponding coulomb efficiency of nearly 100% after 1500 times cycling. The addition of PVP enhances the dispersion of HVO and provides more active sites resulting in the improvement of the battery capacity, showing its rapid reaction kinetics behavior. For comparison, the capacity of HVO cells decline from 160.5 mAh/g to 132.9 mAh/g after the same times cycling, which represents only a retention of 82.0% of the initial capacity. This can be attributed to the repeated insertion/de-insertion process of the zinc ions, which ultimately leads to the structural collapse [33]. Fig. 3f indicates the corresponding charge/discharge curves at various current densities. It can be observed that the capacity decreases as the current density increases. Then we study the work temperature dependent discharge capacities at 5.0 A/g (Fig. 3g). When the temperature is 0 °C, the battery delivers the specific capacity of 180.5 mAh/g. With the increase of work temperature, the discharge capacity improves accordingly owing to the appearance of some thermodynamic reactions [34]. The Zn//HVO-PVP battery presents a specific capacity of 343.5 mAh/g at 1.0 A/g even after 1000 times cycling and a capacity retention of nearly 100% (Fig. 3h).

Then we explore the electrochemical kinetic behavior of the HVO-PVP electrodes. Fig. 4a shows their CV curves at different scanning rates (0.1–0.5 mV/s). As the scan rate increases, they almost retain a similar shape. The redox peaks undergo a gradual shift towards high/low potentials. The logarithmic relationship between the peak current and the sweep speed can be abided by the following equation [35]:

$$i = av^b \tag{1}$$

where a and b are the varied constants. From Fig. 4b, the b values are 1.10, 0.92, 1.03 and 1.00, respectively, the calculated b values are all close to 1. Consequently, the reaction process is predominantly dominated by surface capacitance, which is related to its excellent rate performance [36]. Furthermore, the contribution ratio of capacity and capacitance can be calculated based on the following formula [37]:

$$i(V) = k_1v + k_2v^{1/2} \tag{2}$$

The parameter k_1v represents a surface-controlled process, whereas $k_2v^{1/2}$ denotes a diffusion-controlled one. From Fig. 4c, the capacitance contribution improves from 79.79% to 89.76% as the scanning rate increases. This behavior is conducive to improving the capacity of the battery.

GITT curve is employed to investigate the diffusion coefficient of zinc ions. As shown in Fig. 4d, the calculated result demonstrates the D_{Zn} value (10^{-6} and 10^{-8} cm^2/s) of HVO-PVP electrode materials. Its superior rate benefits the rapid transfer of Zn^{2+} during the redox reaction. Fig. 4e shows the electrochemical impedance spectra (EIS) of the two cathodes. The slopes in the low frequency region are related to zinc-ion diffusion, where the electrode process is dominated by Warburg impedance [38]. The HVO-PVP cathode (R_{ct}, 74 Ω) possesses smaller semicircular diameter than the HVO cathode (R_{ct}, 119 Ω). The resistance of charge transfer is inversely proportional to the kinetics of electrode reaction. The energy density and power density are calculated by the following formulas [39]:

$$E = QU/2m \tag{3}$$

$$P = iU/2m \tag{4}$$

E (Wh/kg) and P (W/kg) refer energy density and power density, respectively. Q represents the discharge capacity, U is the operating voltage, and i is named the discharge current, m denotes the mass loading of the cathode. From Fig. 4f, the power density reaches 3.0 kW/kg when the energy density is 165.8 Wh/kg, which is superior to the previous reports [21,40-43].

Now we investigate the storage mechanism of Zn^{2+} at different charging/discharging stages by ex-situ XRD characterization. Fig. 5a show that the peaks at 26.80° correspond to the (003) crystal planes of $H_{3.78}V_6O_{13}$ phase. During discharging, the diffraction peak shift to a low angle, indicating that the embedding of Zn^{2+} efficiently increase the lattice spacing of the host materials. When charging to 1.4 V, the characteristic peak almost returns to the initial position, demonstrating the excellent reversibility of Zn^{2+} intercalation/deintercalation. In addition, Fig. 5b demonstrates the *ex-situ* XRD patterns at the work temperature of 60 °C. It is found that an additional diffraction peak appears at 12.29°, corresponding to $Zn_3V_2O_7(OH)_2{\cdot}2H_2O$ (ZVOH) phase (JCPDS No. 87–0417). The

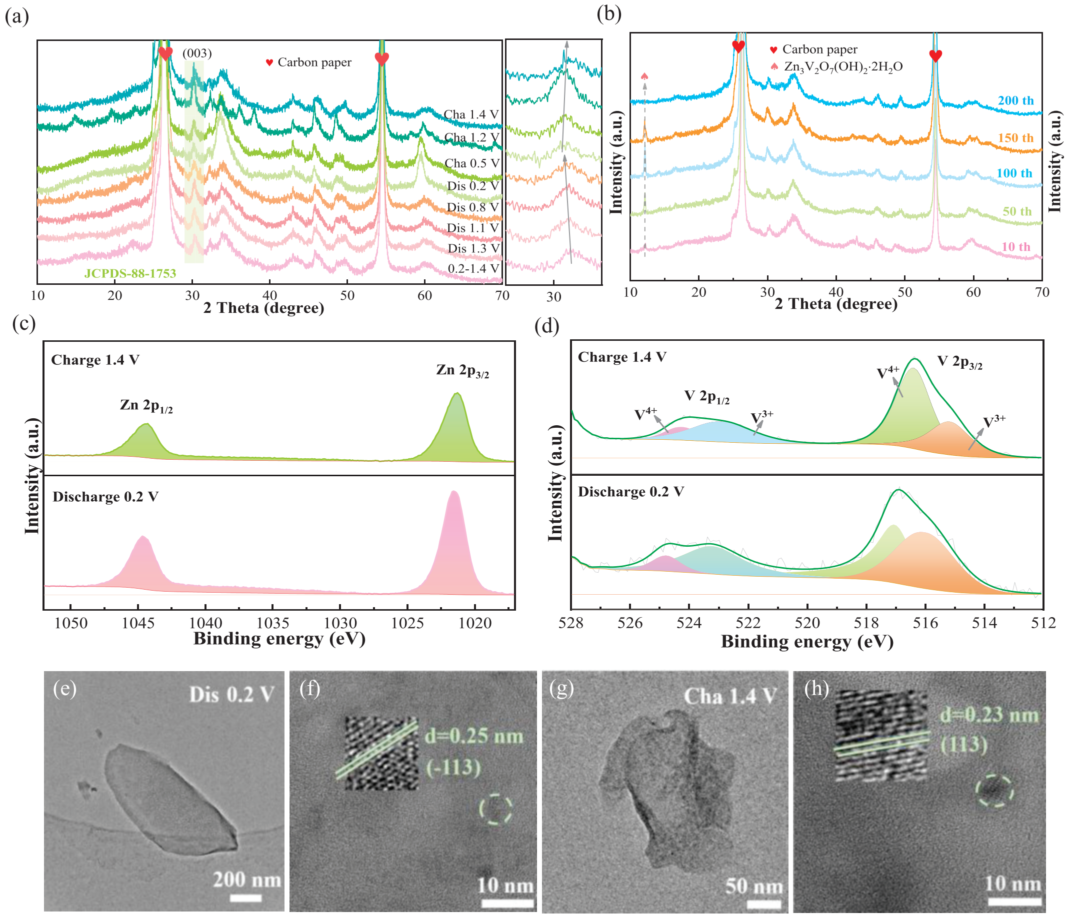

Fig. 5. Structural and morphology characterizations of HVO-PVP samples. (a, b) *Ex-situ* XRD patterns. (c, d) XPS spectra TEM and HRTEM images. (e, f) Discharging at 0.2 V and (g, h) charging at 1.4 V.

formation of ZVOH is ascribed to the strong electrostatic interaction between the embedded Zn^{2+} and the vanadium oxygen layer, which leads to the decreasing of lattice spacing [44].

Finally, XPS spectra are used again to investigate the composition and chemical valence states of the electrodes at different voltages. The Zn 2p spectrum is presented in Fig. 5c. When discharged to 0.2 V, we observe two peaks of Zn $2p_{1/2}$ and $2p_{3/2}$, confirming the insertion of Zn^{2+}. After charging, there are a small part of Zn ions in the HVO-PVP electrode [45]. As shown in Fig. 5d, the V 2p XPS spectra show the presence of V^{4+} and V^{3+} species. After discharging to 0.2 V, there is a significant increasing of the V^{3+} signal, suggesting V^{4+} reduction process after Zn^{2+} insertion [46]. When HVO-PVP electrode reach 1.4 V charged state, the V^{4+} signal is recovered due to the Zn^{2+} de-insertion. It proves the high reversibility of HVO-PVP materials. Moreover, HRTEM is utilized to investigate the structure of the HVO-PVP electrodes (Figs. 5e and f). When discharging to 0.2 V, the lattice spacing of $(\bar{1}13)$ crystal face is extended to 0.250 nm owing to the embedding of Zn^{2+}. In the fully charging state, the corresponding spacing returns to 0.236 nm for the (113) crystal face.

In summary, the HVO-PVP electrode materials have been obtained by a one-step hydrothermal strategy. The addition of PVP surfactant largely increases the specific surface area. It facilitates the insertion and de-insertion of Zn^{2+} in redox reaction process. Moreover, the experimental results prove that the Zn//HVO-PVP batteries possess fast electrochemical reaction kinetics and long-term cycle life. They also achieve excellent energy density (165.8 Wh/kg) and power density (3.0 kW/kg). Also, the assembled cells show superior specific capacity and durability at 0 °C. This synthetic strategy can provide a universal protocol to prepare some other cathode materials for ZIBs in future energy storage devices.

Declaration of competing interest

The authors declare that they have no known competing financial interests or personal relationships that could have appeared to influence the work reported in this paper.

CRediT authorship contribution statement

Chunru Zhao: Writing – original draft, Visualization, Validation, Software, Resources, Methodology, Investigation, Formal analysis, Data curation, Conceptualization. **Yi Liu:** Writing – original draft, Visualization, Validation, Software, Methodology, Formal analysis, Data curation. **Shilong Li:** Validation, Software, Formal analysis, Data curation. **Xiang Wu:** Writing – review & editing, Validation, Supervision, Project administration, Funding acquisition, Conceptualization. **Jinghai Liu:** Visualization, Validation, Funding acquisition.

Acknowledgments

The work is supported by National Natural Science Foundation of China (No. 52172218) and the open research funding of Inner Mongolia Engineering Research Center of Lithium-Sulfur Battery Energy Storage (No. MDK2023084).

References

[1] Y. Liu, Y. Liu, X. Wu, et al., J. Colloid Interface Sci. 628 (2022) 33–40.
[2] Z. Su, R. Wang, H. Fan, et al., Rare Metals 41 (2022) 2844–2852.
[3] V. Srivastava, V. Rantala, P. Mehdipour, et al., Chem. Eng. J. 474 (2023) 145822.
[4] Y. Liu, R. Zhang, J. Wang, Y. Wang, iScience 24 (2021) 102332.
[5] Y. Li, D. Zhang, S. Huang, et al., Energy Environ. Mater. 5 (2022) 823–851.
[6] Z. Peng, Z. Feng, Z. Zhang, et al., J. Energy Chem. 91 (2023) 345–369.
[7] Y. Liu, X. Wu, Chin. Chem. Lett. 33 (2022) 1236–1244.
[8] N. Zhang, J. Wang, T. Yi, et al., Coord. Chem. Rev. 479 (2023) 215009.
[9] C. Li, X. Yun, Y. Chen, et al., Chem. Engin. J. 477 (2023) 146901.
[10] Y. Dai, X. Liao, L. Mai, et al., Adv. Mater. 33 (2021) 2100359.
[11] Y. Zeng, X. Lu, S. Zhang, et al., Angew. Chem. Int. Ed. 60 (2021) 22189–22194.
[12] Z. Liu, G. Pulletikurthi, F. Endres, ACS Appl. Mater. Interfaces 8 (2016) 12158–12164.
[13] S. Yang, H. Lv, Y. Wang, et al., Angew. Chem. Int. Ed. 61 (2022) e2209794.
[14] H. Li, W. Zhang, K. Sun, et al., Adv. Energy Mater. 11 (2021) 2100867.
[15] L. Ye, H. Fu, R. Cao, J. Yang, J. Colloid Interface Sci. 664 (2024) 423–432.
[16] J. Yan, T. Liu, X. Liu, et al., Coord. Chem. Rev. 452 (2021) 214300.
[17] T. Wu, J. Chen, J. Su, J. Colloid Interface Sci. 654 (2023) 308–316.
[18] K. Guan, K. Duan, G. Yang, et al., Mater. Today Adv. 14 (2022) 100230.
[19] W. Jiang, W. Wang, H. Shi, et al., J. Colloid Interface Sci. 647 (2023) 124–133.
[20] S. Li, L. Qin, L. Li, et al., Int. J. Electrochem. Sci. 16 (2021) 210349.
[21] J. Cao, D. Zhang, Y. Yue, et al., Adv. Funct. Mater. 33 (2023) 2307270.
[22] Y. Liu, Y. Zou, M. Guo, et al., Chem. Eng. J. 433 (2022) 133528.
[23] Y. Li, H. Liu, M. Ma, et al., ACS Appl. Mater. Interfaces 16 (2024) 26079–26087.
[24] S. Huang, S. He, H. Qin, X. Hou, ACS Appl. Mater. Interfaces 13 (2021) 44379–44388.
[25] N. Wang, H. Liu, M. Sun, et al., ACS Sustain. Chem. Eng. 12 (2024) 3527–3537.
[26] Y. Liu, Y. Liu, X. Wu, Y. Cho, ACS Sustain. Chem. Eng. 11 (2023) 13298–13305.
[27] Y. Tong, Y. Zang, S. Su, et al., J. Energy Chem. 77 (2023) 269–279.
[28] A. Zhang, R. Zhao, Y. Wang, et al., Angew. Chem. Int. Ed. 62 (2023) e202313163.
[29] Y. Liu, X. Wu, Nano Energy 127 (2024) 109809.
[30] M. Zhao, S. Li, X. Wu, A. Abdukader, Mater. Adv. 5 (2024) 3965–3972.
[31] L. Lin, S. Tian, L. Fang, et al., J. Energy Storage 72 (2023) 108356.
[32] X. Wu, Y. Zhao, C. Yang, G. He, J. Mater. Sci. 50 (2015) 4250–4257.
[33] Y. Liu, Y. Liu, X. Wu, Chin. Chem. Lett. 34 (2023) 107839.
[34] G. Yang, J. Huang, X. Wan, Nano Energy 90 (2021) 106500.
[35] D. Jia, K. Zheng, M. Song, et al., Nano Res. 13 (2020) 215–224.
[36] Y. Liu, Y. Liu, X. Wu, EcoMat 5 (2023) e12409.
[37] Y. Tong, Y. Zang, S. Su, et al., J. Energy Chem. 77 (2023) 269–279.
[38] B. Hong, X. He, H. Yi, C. Hu, Materials (Basel) 13 (2020) 5528.
[39] Y. Liu, A. Umar, X. Wu, Rare Met. 41 (2022) 2985–2991.
[40] S. Li, M. Zhao, D. Zhang, X. Wu, Cryst. Growth Des. 23 (2023) 8156–8162.
[41] J. Cao, T. Ou, S. Geng, et al., J. Colloid Interface Sci. 656 (2024) 495–503.
[42] C. Zhao, Y. Liu, X. Wu, S. Luo, Adv. Sustain. Syst. 8 (2024) 2400077.
[43] S. Zhao, J. Liu, X. Wu, Ionics (Kiel) 29 (2023) 5267–5273.
[44] T. Zhou, Q. Han, X. Yang, et al., Chem. Eng. J. 445 (2022) 136789.
[45] H. Ren, J. Zhang, B. Wang, et al., Rare Met. 41 (2022) 1605–1615.
[46] M. Zhu, H. Wang, W. Lin, et al., Small Struct. 3 (2022) 2200016.